NEUROPHOTONICS

RESEARCH PAPER

Label-free photoacoustic computed tomography of visually evoked responses in the primary visual cortex and four subcortical retinorecipient nuclei of anesthetized mice

Kai-Wei Chang[a], **Xueding Wang**[a,b], **Kwoon Y. Wong**[c,d] and **Guan Xu**[a,c,*]

[a]University of Michigan, Department of Biomedical Engineering, Ann Arbor, Michigan, United States
[b]University of Michigan, Department of Radiology, Ann Arbor, Michigan, United States
[c]University of Michigan, Department of Ophthalmology and Visual Sciences, Ann Arbor, Michigan, United States
[d]University of Michigan, Department of Molecular, Cellular and Developmental Biology, Ann Arbor, Michigan, United States

ABSTRACT. **Significance:** Many techniques exist for screening retinal phenotypes in mouse models in vision research, but significant challenges remain for efficiently probing higher visual centers of the brain. Photoacoustic computed tomography (PACT), with optical sensitivity to hemodynamic response (HR) in brain and ultrasound resolution, provides unique advantages in comprehensively assessing higher visual function in the mouse brain.

Aim: We aim to examine the reliability of PACT in the functional phenotyping of mouse models for vision research.

Approach: A PACT-ultrasound (US) parallel imaging system was established with a one-dimensional (1D) US transducer array and a tunable laser. Imaging was performed at three coronal planes of the brain, covering the primary visual cortex and the four subcortical nuclei, including the superior colliculus, the dorsal lateral geniculate nucleus, the suprachiasmatic nucleus, and the olivary pretectal nucleus. The visual-evoked HR was isolated from background signals using an impulse-based data processing protocol. *rd1* mice with rod/cone degeneration, melanopsin-knockout (mel-KO) mice with photoreceptive ganglion cells that lack intrinsic photosensitivity, and wild-type mice as controls were imaged. The quantitative characteristics of the visual-evoked HR were compared.

Results: Quantitative analysis of the HRs shows significant differences among the three mouse strains: (1) *rd1* mice showed both smaller and slower responses compared with wild type ($n = 10,10$, $p < 0.01$) and (2) mel-KO mice had lower amplitude but not significantly delayed photoresponses than wild-type mice ($n = 10,10$, $p < 0.01$). These results agree with the known visual deficits of the mouse strains.

Conclusions: PACT demonstrated sufficient sensitivity to detecting post-retinal functional deficits.

Keywords: photoacoustic computed tomography; retinal photostimulation; hemodynamic response; photoreceptor degeneration; melanopsin

Paper 24029GR received Apr. 12, 2024; revised Jun. 17, 2024; accepted Jul. 2, 2024; published Jul. 30, 2024.

*Address all correspondence to Guan Xu, guanx@umich.edu

1 Introduction

Mouse models are popular in vision research due to their phylogenetic similarity to humans and the availability of versatile genetic tools.[1] Researchers analyze the phenotypes of various mouse models of human diseases to learn how these diseases might impact visual functions and to assess therapeutic efficacy. Many techniques for screening retinal phenotypes in these mice exist,[2] but significant challenges for efficiently probing higher visual centers of the brain remain. Although microelectrode recording, two-photon imaging, and immunostaining of activity-dependent gene expression provide cellular resolution, these time-inefficient methods are impractical for comprehensive phenotypic screening of the visual system. Thus, many researchers have turned to simple behavioral assays such as the pupillary light reflex and optokinetic reflexes, but these subcortically driven responses do not assess image-forming vision, and rapid functional assays remain unavailable for most visual nuclei.

A promising approach for comprehensively phenotyping the mouse visual system is the imaging of visual-evoked hemodynamic responses (HRs), which are highly correlated to neural activities.[3] Importantly, these volumetric imaging methods can theoretically analyze most if not all of the >20 brain visual areas simultaneously, thereby dramatically boosting the efficiency of post-retinal functional phenotyping of mouse models. Functional magnetic resonance imaging (fMRI), based on the blood-oxygen-level-dependent (BOLD) effect, has sufficient spatial and temporal resolution to resolve hemodynamics in the superior colliculus (SC), dorsal lateral geniculate nucleus (LGd), and primary visual cortex (V1) in mice;[4] however, its high cost and enclosed system configuration restrict applications in vision research with small animals. Functional near-infrared spectroscopy (fNIRS) possesses a contrast mechanism comparable to fMRI, but with higher sensitivity to hemodynamics.[5] fNIRS exhibits excellent mobility and temporal resolution in imaging human brain activities, substantially expanding the scope of brain research in the past decade.[6] With spatial resolution limited by photon diffusion to a few millimeters, fNIRS, however, cannot resolve most visual nuclei in the mouse brain.[5]

Photoacoustic computed tomography (PACT) breaks the photon diffusion limit by combining the contrast mechanism of fNIRS and the spatial resolution of ultrasound imaging. PACT systems can image up to hundreds of frames per second[7] with a resolution of about 100 μm at a depth of 1 cm.[8] PACT has revealed resting-state functional connectivity in multiple cortical areas[9,10] and captured cortical responses to intense electrical stimulations with[11] or without optical contrast agents.[12] PACT has successfully recorded visual responses in V1 cortex of mice[13] and rats[14,15] and more recently in the mouse SC.[16] In PACT-US parallel imaging, the PACT images are naturally co-registered with the US images as the transducer array acquires both simultaneously, thereby allowing the HR to be easily superimposed onto the brain anatomies revealed by US imaging.

Our recent pilot study confirmed the feasibility of PACT-US parallel imaging to capture visually evoked HRs in V1 and SC of wild-type mice.[16] The present study used a linear array with a mechanical translation to cover major visual regions of high interest to researchers, including the V1, SC, LGd, suprachiasmatic nucleus (SCN), and olivary pretectal nucleus (OPN). In addition, we established a data processing method for isolating the visual-evoked responses from background signals. Rod/cone-degenerate (*rd1*) and melanopsin-knockout (mel-KO) mice were used to investigate the performance of our system.

2 Materials and Methods

2.1 Mouse Preparation

All animal procedures were approved by the Institutional Animal Care and Use Committee at the University of Michigan. Three mouse strains were used: homozygous *rd1* mice, mel-KO mice,[17] and C57BL/6 wild-type mice. All animals were aged 2 to 3 months, and both sexes were studied to avoid any sex-related bias. Animals were kept in a 12-h light/dark cycle, with PACT conducted during the light phase. Under anesthesia by isoflurane (4%) and analgesia by carprofen (5 mg/kg s.c.) plus topical bupivacaine (2 mg/kg), the scalp of the animal was removed to minimize optical and acoustic attenuation, and the skull was slightly thinned using a micro-drill to reduce acoustic attenuation.[18,19] The mouse was then returned to its housing cage to recover from the surgery and to dark-adapt overnight. Just before PACT imaging, the mouse was anesthetized by

1% isoflurane in conjunction with acepromazine (5 mg/kg i.p.)[20] and secured to a multi-axis translation stage with its cortex surface aligned perpendicular to the imaging plane. Imaging and photostimulation were performed as described in Secs. 2.2 and 2.3. At the end of the imaging session, the mouse was euthanized using cervical dislocation while still under anesthesia, in accordance with the guidelines of the Unit for Laboratory Animal Medicine at the University of Michigan.

2.2 Imaging System

Figure 1(a) shows a schematic of our PACT system for real-time brain imaging. This system was used in our previous study[16] and is briefly described here. A neodymium-doped yttrium aluminum garnet laser-pumped optical parametric oscillator (Phocus MOBILE, OPOTEK Inc., Carlsbad, California, United States) was used as the excitation source, with a pulse duration of 5 to 7 ns, a pulse repetition rate of 10 Hz, and a pulse energy variation below 5%. A 797-nm laser beam was delivered through a bifurcated, multimode fiber bundle with fiber tips attached on both sides of a linear 256-element ultrasonic array (GE L8-18i) with a central frequency of 10 MHz. A 797-nm laser wavelength was chosen because (1) mouse retinal photoreceptors are insensitive to near-infrared wavelengths,[21,22] so the imaging illumination would not interfere with the visual stimulation and (2) at 797 nm, the oxygenated and deoxygenated hemoglobin have the same absorption coefficients, thereby facilitating the calculation of total hemoglobin levels. The US array integrated with fiber optics was positioned 1 cm away from the skull surface. The maximum optical fluence at the skull surface was ~20 mJ/cm^2, below the American National Standards Institute safety limit of 31 mJ/cm^2 at 797 nm.[23] The US transducer array was mechanically translated among three imaging planes containing the brain regions of interest, at a frame rate of ~3.3 Hz for each imaging plane. The PA signals were digitalized and sampled at 40 MHz with a Vantage 256 ultrasound research system (Verasonics, Redmond, Washington, United States), which has an axial resolution of 150 μm and a lateral resolution of 150 μm at a 2-cm imaging depth, roughly corresponding to the distance between the US array and the bottom of the mouse brain.

2.3 Retinal Photostimulation

The visual stimulus was broadband white light generated by a fiber-optic halogen illuminator (HL150-B, AmScope, Old Bridge, New Jersey, United States) flickering at 1 Hz and positioned about 5 cm from each eye, producing an irradiance of ~16 mW/cm^2 at the cornea. Before

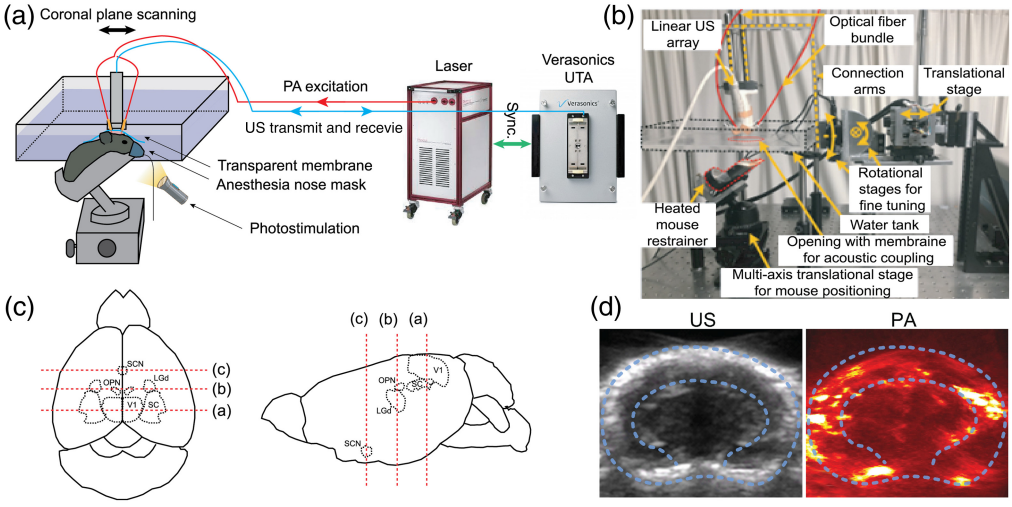

Fig. 1 System overview. (a) A schematic diagram of the PACT system. (b) A photograph of the system and the translational stage for coronal plane imaging. (c) The positions of the targeted brain nuclei: V1, primary visual cortex; SC, superior colliculus; LGd, dorsal lateral geniculate nucleus; OPN, olivary pretectal nucleus; and SCN, suprachiasmatic nucleus. The three imaging planes are indicated with red dashed lines. (d) Representative US and PACT images acquired by the system. The dashed contours illustrate the contours of the skull and inner brain.

photostimulation, the dark-adapted mouse was kept in constant darkness for 10 min for baseline measurement. Then, both eyes were exposed to the flickering stimulus simultaneously for 10 s, followed by another 10 min in darkness, during which PACT imaging continued to monitor hemodynamic recovery from the photoresponse.

2.4 Image Reconstruction and Signal Processing

The PACT images were reconstructed using a delay-and-sum beamforming algorithm from the acquired signals. The temporal trace of each pixel was extracted from the PACT video as 200 consecutive frames covering a 1-min period, with 67 frames (i.e., 20 s) immediately before stimulation, 33 frames during stimulation, and 100 frames immediately after stimulation. Each 200-frame trace was first detrended by subtracting the linear fitting line of the pre-stimulation temporal trace to remove the systematic shift from the detected signal. Then, it was normalized by the root mean square of the signal strength of the original pre-stimulation temporal trace before subtraction, resulting in the baseline-subtracted and normalized PA signals ($\Delta PA/PA$). A spatial moving average of 3×3 pixels and a temporal forward-moving average of eight frames (2.7 s) were also applied to filter out the noise from random fluctuations. After signal processing, the vessel features of the PACT images were removed, while the temporal traces of the PA amplitude changes remained.

2.5 Isolation of the HR

We established a data processing protocol to isolate the HR from the background noise in PA signals, building upon established techniques in fMRI and fNIRS.

A bandpass filter ranging from 0.01 to 1.25 Hz is applied to the frequency domain spectra of the PA signals. This step is crucial for reducing repetitive noises stemming from physiological activities such as respiration and heartbeats, as well as low-frequency baseline signals.[24] We then implement a Kalman filter to eliminate autocorrelated measurement noises.[24]

To model the visual-evoked HR, we use linear basis function modeling based on a fixed canonical-shaped HR,[25–27] a model commonly utilized in fMRI[28] and fNIRS.[29,30] This function models the impulse HR to neuronal activation, as shown in Fig. 2(a). The impulse HR is convolved with our photostimulation sequence, forming the basis function, as shown in Fig. 2(b).

The HR is then modeled as a linear combination of a basis set, following standard methods.[31–36] The model is expressed as

$$y_t = \hat{\beta}_0 + \hat{\beta}_1 x_t + \hat{\beta}_2 \frac{\partial x_t}{\partial t} + \hat{\beta}_3 \frac{\partial^2 x_t}{\partial^2 t} + \varepsilon_t,$$

where $\hat{\beta}_0$ is a constant bias, $\hat{\beta}_1 x_t + \hat{\beta}_2 \frac{\partial x_t}{\partial t} + \hat{\beta}_3 \frac{\partial^2 x_t}{\partial^2 t}$ represents the second-order Taylor expansion of the basis function, and ε_t is a noise term. Considering that some mouse strains with visual impairments exhibit delayed responses, we fit the temporal traces at each pixel in the PA image to a series of basis sets with 1-s shifts by adjusting $\hat{\beta}_i$. The basis set yielding the least fitting error and the lowest p-value in the linear fit is selected as the isolated HR, as shown in the red trace in Fig. 2(c).

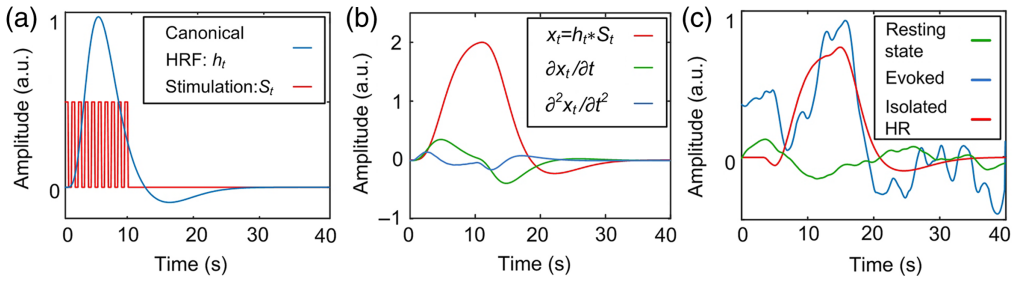

Fig. 2 HR isolation from PA signals. (a) Canonical function and visual stimulation sequence. (b) A basis set derived from panel (a). (c) Resting state and visually evoked temporal trace in PA image and the isolated HR.

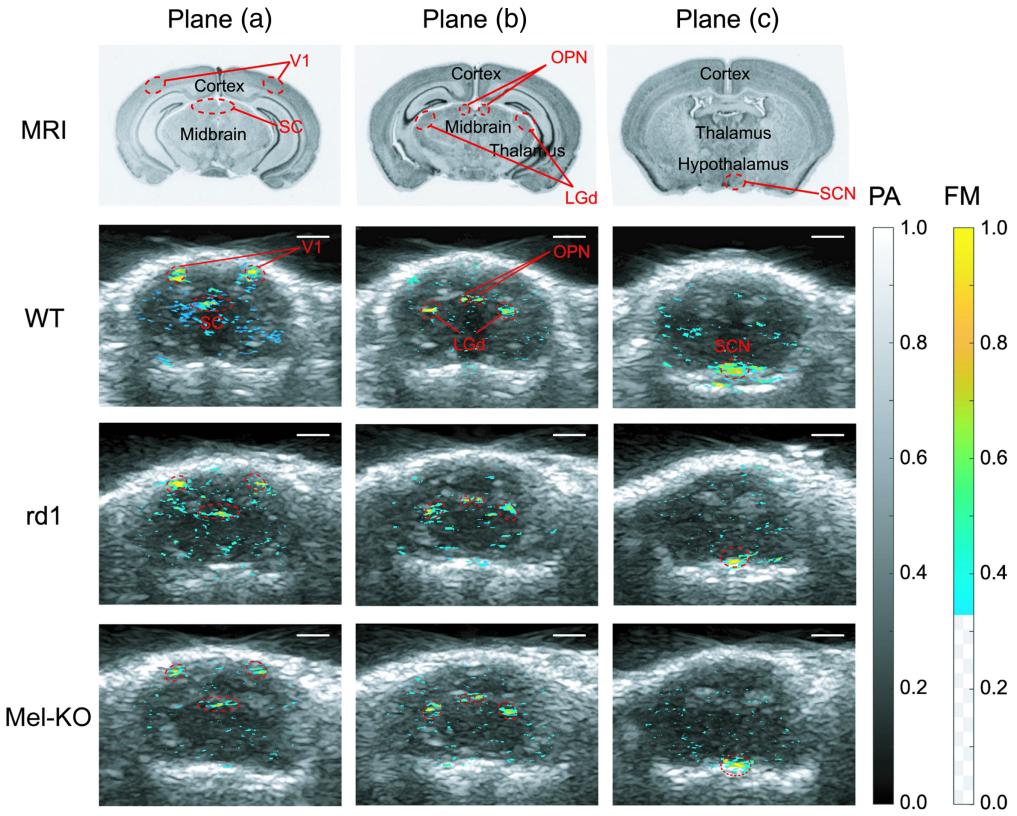

Fig. 3 Visual regions of interest and the FMs acquired by the PACT-US system. The three columns of images correspond to the three imaging planes in this study. Row 1: MRI images from the Allen Brain Atlas at the imaging planes. The visual regions of interest are marked with red dashed ovals. Rows 2 to 4 are representative visual-evoked FMs derived from PA images overlaid on the US images in wild-type, *rd1*, and mel-KO mice, respectively. The contours of the targeted nuclei are marked with red dashed ovals. Scale bars: 2 mm.

3 Results

3.1 Functional Maps of Visual-Evoked Hemodynamic Changes

Figure 3 row 1 shows MRI images from the Allen Brain Atlas (Allen Institute for Brain Sciences, Seattle, Washington, United States). By comparing with anatomies in those images, the five visual areas of interest were located in the US images. To generate functional maps (FMs, color-coded pixels in Fig. 3 rows 2 to 4), we calculated the maximum relative variations of the averaged signal amplitude at each pixel of the temporal PA images during and after stimulation (20 to 60 s) compared to the averaged signal amplitude before stimulation (0 to 20 s). The color-coded pixels were co-registered with the US images to confirm that the areas with the most robust visually evoked hemodynamic changes matched the locations of the five brain regions of interest (Fig. 3).

3.2 Temporal Traces of Visually Evoked Hemodynamic Changes

Five males and five females of each mouse strain were studied, and all five targeted brain regions were examined in each mouse. The average temporal traces are shown in Fig. 4, and the average isolated HRs are in Fig. 5. To quantify visual deficits in *rd1* and mel-KO mice, we measured the peak amplitude and latency of the isolated HRs, as illustrated in Fig. 5(a): the peak amplitude was calculated by measuring the difference between the peak PA signal intensity and the mean pre-stimulation intensity, and the peak latency was measured as the time at which the signal reached the maximum intensity after the onset of photostimulation.

Figure 6 shows the statistical analysis of the quantitative measurements from the three genotypes. In all of the targeted nuclei, the peak amplitudes of both *rd1* and mel-KO mice were significantly lower than wild-type mice, but only *rd1* mice had significantly longer response

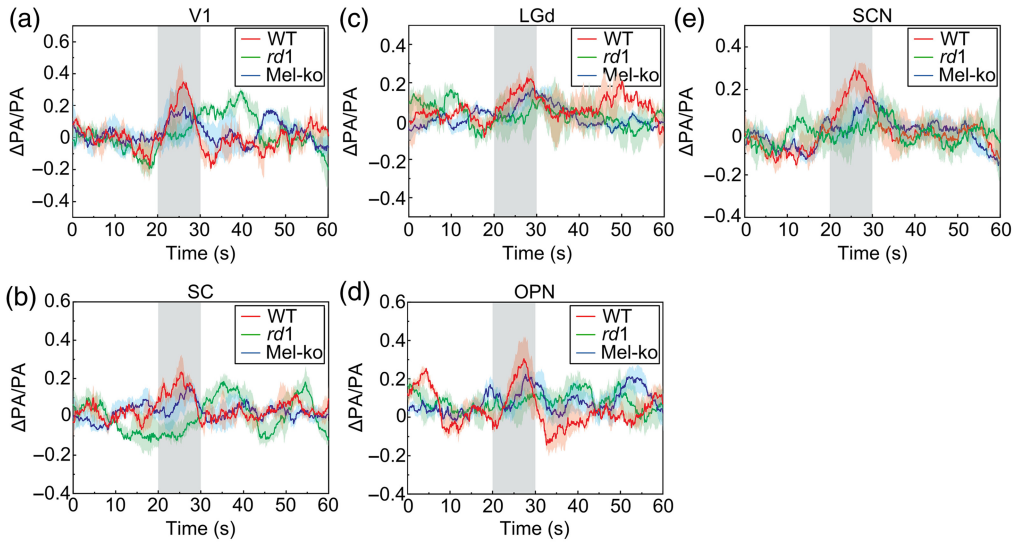

Fig. 4 Visually evoked hemodynamic changes detected in V1 (a), SC (b), LGd (c), OPN (d), and SCN (e) of the three mouse strains. Shaded areas at 20 to 30 s represent the period of stimulation. In each panel, each trace plots the mean PA signals (ΔPA/PA) measured over the 60-s protocol for one of the mouse strains: 10 wild-type mice (red), 10 *rd1* mice (green), and 10 mel-KO mice (blue). To generate each trace, the single pixels with the highest visual-evoked changes were first identified in the corresponding visual region of each mouse, with the mean pre-stimulation PA signals normalized to zero, and the 10 mice's temporal traces were averaged. The standard deviations of the PA signals are shown as the upper and lower bounds of the traces.

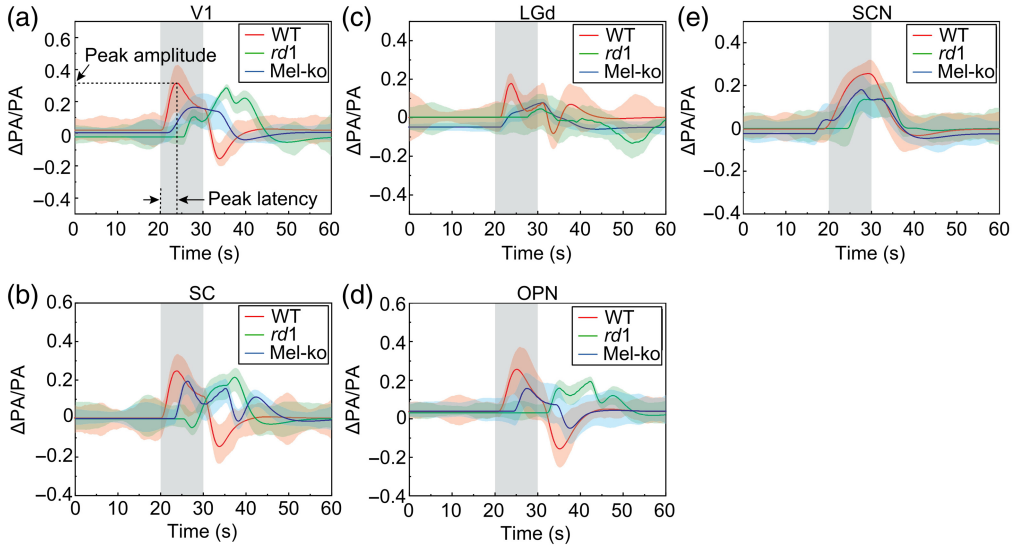

Fig. 5 Isolated visual-evoked hemodynamic changes in V1 (a), SC (b), LGd (c), OPN (d), and SCN (e) of the three mouse strains. The traces are population-averaged temporal traces of the background-subtracted and normalized PA signals (ΔPA/PA) for single pixels with the highest functional changes located in the targeted brain areas of 10 wild-type mice (red), 10 *rd1* mice (green), and 10 mel-KO mice (blue). The standard deviations of the temporal traces are shown as the upper and lower bounds of the traces. Shaded areas represent the period of stimulation. Two properties of the visual-evoked responses were quantified as illustrated in panel (a), and the results are presented in Fig. 6.

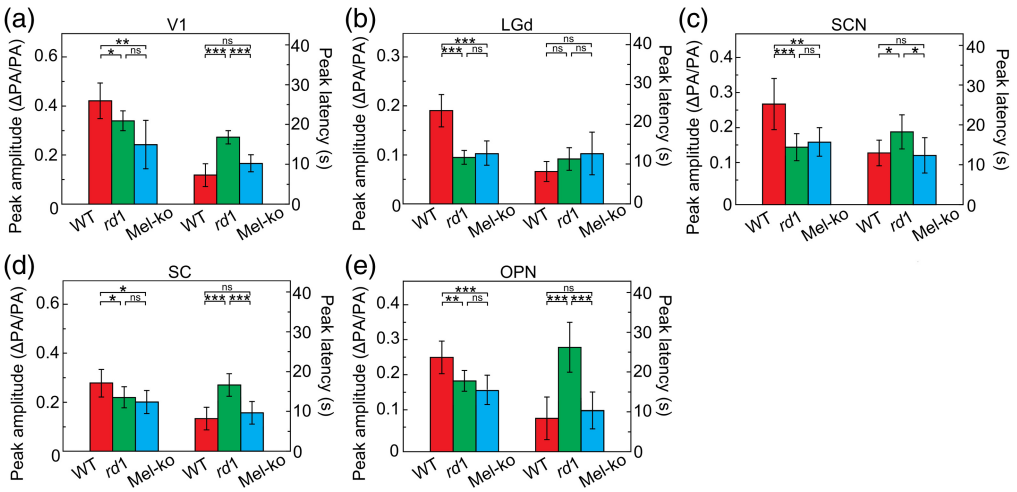

Fig. 6 Statistical analysis comparing the peak amplitudes and peak latencies of the targeted nuclei (a)–(e) for wild-type mice (red columns), *rd1* mice (green columns), and mel-KO mice (blue columns). $^{*}p < 0.05$ ($n = 10,10$); $^{**}p < 0.01$ ($n = 10,10$); $^{***}p < 0.005$ ($n = 10,10$).

latencies compared with wild-type mice, specifically in V1, SC, OPN, and SCN [Figs. 6(a), 6(b), 6(d), and 6(e)].

4 Discussion

Our PACT-US system effectively delineated visual-evoked responses in V1 and several subcortical nuclei in the mouse brain. The quantitative evaluation of temporal traces from these functionally important regions revealed differences in visual-evoked HR among wild-type, *rd1*, and mel-KO mice. These differences are largely congruent with expectations as follows: (1) because all five areas receive input from photoreceptive ganglion cells,[37–41] mel-KO mice had lower amplitude photoresponses than wild type; (2) the residual responses in mel-KO were driven by rod/cone photoreceptors and thus were not significantly delayed compared with wild type; and (3) *rd1* mice, using only melanopsin, which responds to light sluggishly,[42] showed both smaller and slower responses compared with wild type. Such agreement underscores the potential of this imaging technique in high-throughput phenotyping of the mouse brain.

Currently, the frame rate of the imaging system is 3.3 Hz at each imaging plane. The temporal traces in Figs. 4 and 5 show that this frame rate can capture the HR waveform with sufficient fidelity to detect the reduced response kinetics in *rd1* mice. The limiting factors of the current imaging system include the 2D imaging ability, the small number of imaging planes, the mechanical translation between the imaging planes, and the laser repetition rate. The frame rate can be potentially improved using 2D US transducer arrays for 3D imaging without mechanical translation and lasers with higher repetitional rates. A substantial increase in frame rate will allow more temporal averaging to increase the signal-to-noise ratios and the potential detection of more subtle features in HRs such as the overshoot and undershoot observed in fMRI.[43,44]

The 797-nm optical wavelength was used for PA excitation in this study to target total hemoglobin content. All of the quantitative analysis was based on PA signal changes. The optical attenuation along the penetration was not considered in this study. This approach is comparable to fMRI sensitized to the contrast of cerebral blood volume, which has been shown to have greater spatial specificity of neural activity detection compared with BOLD contrast.[45] The measurement of oxygenation with PACT would require at least two optical wavelengths, which attenuate differently as they penetrate the brain. Signal intensity compensation using optical energy distribution at each wavelength, as was done in previous studies,[46,47] would have to be performed for quantitative analysis.

The temporal traces in Fig. 4 showed changes with ~40% fluctuations. Considering that there is an ~10% system fluctuation at the resting state, the visually evoked signal has an

~30% fractional change, which is comparable to a previous study.[48] The post-stimulus undershoot has been observed in fMRI and fNIR signals in both humans and animals.[43] The empirical canonical HR function integrates such features.[25–27] We believe that the negative changes of the HR in this study are real and captured by the canonical function fitting. In our future work, we will seek to define the true hemodynamics response function in the visual region using larger cohorts and animals and improve our results. We include this information in the discussion section.

A unique advantage of PACT in small animals, similar to that of fNIRS in human subjects,[49] is the feasibility of integrating all imaging components into a small and lightweight wearable 3D platform for brain imaging. Such a platform would allow for volumetric imaging of multiple visual nuclei in mice without anesthesia or restraining, thereby avoiding anesthesia/restraint-induced HR alterations as well as facilitating longer-term recordings. Numerous studies have reported that anesthesia inhibits neural responses in the visual system. For instance, we have shown that raising the isoflurane level from 0.5% to 1% dramatically slows pupillary light reflexes in mice.[20] Other labs have found anesthesia to render SCN photoresponses significantly weaker[50] and more transient[51,52] and to disrupt higher visual processing.[53–57] PACT imaging of free-moving animals would enable studying visual responses under more normal physiologic conditions.

5 Conclusion

This study has established a label-free, high-resolution PACT system capable of real-time monitoring of visual-evoked HRs across different brain regions in anesthetized mice. The system successfully identified hemodynamic changes in V1, SC, LGd, OPN, and SCN in response to retinal photostimulation. Considering that (1) these are the only five visual regions the we have attempted to date and all were imaged successfully and (2) the SCN is likely one of the most challenging nuclei to image given its depth and small size, it seems reasonable to expect PACT to be capable of imaging most of the other visual areas in the mouse brain. Comparisons among the responses in *rd1*, mel-KO, and wild-type mice validated the sensitivity of this technique in discerning significant variances in response amplitudes and latencies. Such findings highlight the potential of our system to detect post-retinal visual deficits in various mouse models, filling a significant technological gap in vision research.

Disclosures

The authors declare no conflicts of interest.

Code and Data Availability

Data and data processing codes underlying the results presented in this paper are stored at an online archiving location that may be accessed from the authors upon reasonable request.

Acknowledgments

We thank Zhongming Liu with the Department of Biomedical Engineering at the University of Michigan for his assistance in establishing the HR isolation protocol. This research was supported in part by the National Institutes of Health (Grant Nos. R37CA222829, R01DK125687, and 5P30EY007003) and the Mcubed grant through the University of Michigan.

References

1. J. Won et al., "Mouse model resources for vision research," *J. Ophthalmol.* **2011**, 391384 (2011).
2. J. Won et al., "Translational vision research models program," in *Retinal Degenerative Diseases*, M. LaVail et al., Eds., pp. 391–397, Springer US (2012).
3. X. Wan et al., "The neural basis of the hemodynamic response nonlinearity in human primary visual cortex: implications for neurovascular coupling mechanism," *NeuroImage* **32**, 616–625 (2006).
4. A. Niranjan et al., "fMRI mapping of the visual system in the mouse brain with interleaved snapshot GE-EPI," *NeuroImage* **139**, 337–345 (2016).
5. G. Strangman et al., "A quantitative comparison of simultaneous BOLD fMRI and NIRS recordings during functional brain activation," *NeuroImage* **17**, 719–731 (2002).

6. H. Ayaz et al., "Optical imaging and spectroscopy for the study of the human brain: status report," *Neurophotonics* **9**, S24001 (2022).
7. D. Das et al., "Label-free high frame rate imaging of circulating blood clots using a dual modal ultrasound and photoacoustic system," *J. Biophotonics* **14**, e202000371 (2021).
8. L. V. Wang and S. Hu, "Photoacoustic tomography: in vivo imaging from organelles to organs," *Science* **335**, 1458–1462 (2012).
9. M. Nasiriavanaki et al., "High-resolution photoacoustic tomography of resting-state functional connectivity in the mouse brain," *Proc. Natl. Acad. Sci.* **111**, 21 (2014).
10. P. Zhang et al., "High-resolution deep functional imaging of the whole mouse brain by photoacoustic computed tomography in vivo," *J. Biophotonics* **11**, e201700024 (2018).
11. J. Yao et al., "Noninvasive photoacoustic computed tomography of mouse brain metabolism in vivo," *NeuroImage* **64**, 257–266 (2013).
12. S. Gottschalk et al., "Rapid volumetric optoacoustic imaging of neural dynamics across the mouse brain," *Nat. Biomed. Eng.* **3**, 392–401 (2019).
13. K.-W. Chang et al., "Label-free photoacoustic computed tomography of mouse cortical responses to retinal photostimulation using a pair-wise correlation map," *Biomed. Opt. Express* **13**, 1017–1025 (2022).
14. J. Tang et al., "Noninvasive high-speed photoacoustic tomography of cerebral hemodynamics in awake-moving rats," *J. Cereb. Blood Flow Metab.* **35**, 1224–1232 (2015).
15. J. Tang et al., "Wearable 3-D photoacoustic tomography for functional brain imaging in behaving rats," *Sci. Rep.* **6**, 25470 (2016).
16. K.-W. Chang et al., "Photoacoustic imaging of visually evoked cortical and subcortical hemodynamic activity in mouse brain: feasibility study with piezoelectric and capacitive micromachined ultrasonic transducer (CMUT) arrays," *Biomed. Opt. Express* **14**, 6283–6290 (2023).
17. J. L. Ecker et al., "Melanopsin-expressing retinal ganglion-cell photoreceptors: cellular diversity and role in pattern vision," *Neuron* **67**, 49–60 (2010).
18. A. Y. Shih et al., "A polished and reinforced thinned-skull window for long-term imaging of the mouse brain," *J. Visualized Exp.* **61**, e3742 (2012).
19. G. Yang et al., "Thinned-skull cranial window technique for long-term imaging of the cortex in live mice," *Nat. Protoc.* **5**, 201–208 (2010).
20. S. S. Eckley et al., "Acepromazine and chlorpromazine as pharmaceutical-grade alternatives to chlorprothixene for pupillary light reflex imaging in mice," *J. Amer. Assoc. Lab Anim. Sci.* **59**, 197–203 (2020).
21. Y. Ma et al., "Mammalian near-infrared image vision through injectable and self-powered retinal nanoantennae," *Cell* **177**, 243–255.e15 (2019).
22. D. G. Luo et al., "Activation of visual pigments by light and heat," *Science* **332**, 1307–1312 (2011).
23. A. Standard Z136.1, *American National Standard for the Safe Use of Lasers*, American National Standards Institute, Inc., New York (1993).
24. L. Gagnon et al., "Improved recovery of the hemodynamic response in diffuse optical imaging using short optode separations and state-space modeling," *NeuroImage* **56**, 1362–1371 (2011).
25. R. Henson and K. Friston, "Convolution models for fMRI," in *Statistical parametric mapping: the analysis of functional brain images*, K. Friston et al., Eds., pp. 178–192, Academic Press (2007).
26. T. Jin and S.-G. Kim, "Cortical layer-dependent dynamic blood oxygenation, cerebral blood flow and cerebral blood volume responses during visual stimulation," *NeuroImage* **43**, 1–9 (2008).
27. M. Havlicek et al., "Determining excitatory and inhibitory neuronal activity from multimodal fMRI data using a generative hemodynamic model," *Front. Neurosci.* **11**, 616 (2017).
28. M. J. McKeown, L. K. Hansen, and T. J. Sejnowsk, "Independent component analysis of functional MRI: what is signal and what is noise?" *Curr. Opin. Neurobiol.* **13**, 620–629 (2003).
29. E. Hernandez-Martin et al., "Diffuse optical tomography to measure functional changes during motor tasks: a motor imagery study," *Biomed. Opt. Express* **11**, 6049–6067 (2020).
30. Z. Cai et al., "Diffuse optical reconstructions of functional near infrared spectroscopy data using maximum entropy on the mean," *Sci. Rep.* **12**, 2316 (2022).
31. K. Han et al., "Variational autoencoder: an unsupervised model for encoding and decoding fMRI activity in visual cortex," *NeuroImage* **198**, 125–136 (2019).
32. F. Cignetti et al., "Pros and cons of using the informed basis set to account for hemodynamic response variability with developmental data," *Front. Neurosci.* **10**, 322 (2016).
33. D. H. Kim et al., "Increasing motor cortex activation during grasping via novel robotic mirror hand therapy: a pilot fNIRS study," *J. NeuroEng. Rehabil.* **19**, 8 (2022).
34. V. D. Calhoun et al., "fMRI analysis with the general linear model: removal of latency-induced amplitude bias by incorporation of hemodynamic derivative terms," *NeuroImage* **22**, 252–257 (2004).
35. H. Lambers et al., "A cortical rat hemodynamic response function for improved detection of BOLD activation under common experimental conditions," *NeuroImage* **208**, 116446 (2020).

36. M. A. Lindquist et al., "Modeling the hemodynamic response function in fMRI: efficiency, bias and mis-modeling," *NeuroImage* **45**, S187–S198 (2009).
37. A. D. Güler et al., "Melanopsin cells are the principal conduits for rod-cone input to non-image-forming vision," *Nature* **453**, 102–105 (2008).
38. D. Göz et al., "Targeted destruction of photosensitive retinal ganglion cells with a saporin conjugate alters the effects of light on mouse circadian rhythms," *PLoS One* **3**, e3153 (2008).
39. M. Hatori et al., "Inducible ablation of melanopsin-expressing retinal ganglion cells reveals their central role in non-image forming visual responses," *PLoS One* **3**, e2451 (2008).
40. X. Zhao et al., "Photoresponse diversity among the five types of intrinsically photosensitive retinal ganglion cells," *J. Physiol.* **592**, 1619–1636 (2014).
41. T. M. Brown et al., "Melanopsin contributions to irradiance coding in the thalamo-cortical visual system," *PLoS Biol.* **8**, e1000558 (2010).
42. D. M. Berson, F. A. Dunn, and M. Takao, "Phototransduction by retinal ganglion cells that set the circadian clock," *Science* **295**, 1070–1073 (2002).
43. M. L. Schroeter et al., "Investigating the post-stimulus undershoot of the BOLD signal—a simultaneous fMRI and fNIRS study," *NeuroImage* **30**, 349–358 (2006).
44. P. C. M. van Zijl, J. Hua, and H. Lu, "The BOLD post-stimulus undershoot, one of the most debated issues in fMRI," *NeuroImage* **62**, 1092–1102 (2012).
45. F. Zhao et al., "Spatial specificity of cerebral blood volume-weighted fMRI responses at columnar resolution," *NeuroImage* **27**, 416–424 (2005).
46. B. T. Cox et al., "Two-dimensional quantitative photoacoustic image reconstruction of absorption distributions in scattering media by use of a simple iterative method," *Appl. Opt.* **45**, 1866–1875 (2006).
47. B. Cox et al., "Quantitative spectroscopic photoacoustic imaging: a review," *J. Biomed. Opt.* **17**, 061202 (2012).
48. J. Yao et al., "High-speed label-free functional photoacoustic microscopy of mouse brain in action," *Nat. Methods* **12**, 407–410 (2015).
49. A. von Lühmann et al., "Toward Neuroscience of the Everyday World (NEW) using functional near-infrared spectroscopy," *Curr. Opin. Biomed. Eng.* **18**, 100272 (2021).
50. J. H. Meijer et al., "Light responsiveness of the suprachiasmatic nucleus: long-term multiunit and single-unit recordings in freely moving rats," *J. Neurosci.* **18**, 9078–9087 (1998).
51. H. C. van Diepen et al., "Irradiance encoding in the suprachiasmatic nuclei by rod and cone photoreceptors," *FASEB J.* **27**, 4204–4212 (2013).
52. E. Drouyer et al., "Responses of suprachiasmatic nucleus neurons to light and dark adaptation: relative contributions of melanopsin and rod–cone inputs," *J. Neurosci.* **27**, 9623–9631 (2007).
53. A. M. Ghita et al., "Analysis of the visual evoked potential in anesthesia with sevoflurane and chloral hydrate: (variability of amplitudes, latencies and morphology of VEP with the depth of anesthesia)," *J. Med. Life* **6**, 214–225 (2013).
54. J. J. Nassi, S. G. Lomber, and R. T. Born, "Corticocortical feedback contributes to surround suppression in V1 of the alert primate," *J. Neurosci.* **33**, 8504–8517 (2013).
55. F. Briggs and W. M. Usrey, "Corticogeniculate feedback and visual processing in the primate," *J. Physiol.* **589**, 33–40 (2011).
56. H. Lee et al., "Differential effect of anesthesia on visual cortex neurons with diverse population coupling," *Neuroscience* **458**, 108–119 (2021).
57. V. A. F. Lamme, K. Zipser, and H. Spekreijse, "Figure-ground activity in primary visual cortex is suppressed by anesthesia," *Proc. Natl. Acad. Sci.* **95**, 3263–3268 (1998).

Biographies of the authors are not available.